Theory, Simulation and Millimeter-Wave Measurement of the Operating and Parasitic Modes in a High Loss Dielectric Loaded Gyrotron Traveling Wave Amplifier

Guo Liu, Weijie Wang*, Wei Jiang, Yelei Yao, Jianxun Wang, and Yong Luo

(*Invited*)

Abstract—In the gyrotron traveling wave amplifier (gyro-TWA), high loss dielectric materials loaded in a cylindrical waveguide are adopted to suppress the unwanted parasitic oscillations. It is of great importance to accurately understand the relative permittivity ϵ_r and $\tan\delta$ for studying the microwave and millimeter wave dispersion, and loss properties of a specific mode. The high lossy dielectric loaded circuits of the gyro-TWAs made of the BeO-SiC ceramic are theoretical calculated, simulated, and measured. The field distribution, dispersion, and loss properties of three different dielectric loaded circular HE_{12}^d, HE_{22}^d, and TE_{02}^d modes (corresponding to the TE_{11}, TE_{21}, and TE_{01} modes in the smooth hollow cylindrical waveguide respectively) in different frequency bands are respectively investigated. The theoretical analysis, simulation, and measurement results have a good agreement. This work has clear guiding significance for the stable work of gyro-TWAs.

1. INTRODUCTION

Gyrotron traveling wave amplifiers (gyro-TWAs) have been proved to be very promising vacuum electronic sources in the microwave, millimeter, and terahertz wavelengths due to their high output power and broad operating bandwidth [1]. During the last several decades, different beam-wave interaction configurations for the gyro-TWAs have been explored, such as the dielectric loaded (DL) circuit [2–6], helically corrugated waveguide [7–10], confocal [11], and photonic band gaps waveguides [12]. Of all the beam-wave interaction configurations, high loss DL circuit has been widely used to design the gyro-TWA because of its merits of strong attenuation ability to parasitic modes, which allows the gyro-TWA operating with a very high gain [13, 14]. This feature makes it possible to apply in the terahertz band [15–17]. Based on the high loss DL circuit, at the University of Electronic Science and Technology of China (UESTC), a series of gyro-TWAs covering X, Ku, Ka, Q, and W bands has been successfully developed [5, 14, 18–22]. In order to suppress the backward wave TE_{11} and TE_{21} mode oscillations and TE_{01} mode oscillation at the cutoff frequency in the gyro-TWA, a high loss DL circuit made from BeO-SiC ceramic was adopted. In the design, the thickness and dielectric properties of the BeO-SiC material are respectively optimized so that the electric field patterns and dispersion properties are almost the same as the smooth cylindrical waveguide. In addition, the DL circuit should have enough loss to avoid the unwanted modes oscillations. Meanwhile, the high loss dielectric material should have a high thermal conductivity, which can allow the gyro-TWA working at a high average power or continuous wave state. Therefore, it is very important to investigate the dispersion, loss, and electric field distributions of the wanted and unwanted DL circuit modes.

In this paper, a cylindrical DL circuit used in a Q-band gyro-TWA [5] is studied in detail. The circuit dispersion, loss properties, and mode patterns of different modes in the DL circuit are respectively theoretically calculated, and good agreement with the millimeter-wave measurement has been reported. Section 2 presents the physical model and the field matching theory of the DL circuit. Section 3 gives the compared results of the dispersion and loss from theoretical calculation and simulation. Besides, the DL characteristics versus lossy dielectric thickness are also presented. Section 4 demonstrates the vector network analyzer (VNA) measurement and the near field mode pattern scanning results. Finally, a brief conclusion is drawn in Section 5.

2. THEORY OF THE DIELECTRIC LOADED WAVEGUIDE

Generally, a high loss DL circuit in a gyro-TWA is adopted to suppress the backward wave oscillations of parasitic modes and the self oscillation of the operating mode near the cutoff frequency. Figs. 1(a) and (b) present the front and side views of the DL circuit. The dielectric loaded circular waveguide can be divided into two regions. Region 1 is the inner vacuum region with permittivity $\epsilon_1 = \epsilon_0$ and permeability $\mu_1 = \mu_0$, whose radius is R. It is surrounded by the dielectric with the thickness t, permittivity $\epsilon_2 = \epsilon_0\epsilon_r$, and permeability $\mu_2 = \mu_0\mu_r$. The outer surface of the dielectric ceramic is covered by copper. In the TE_{01} mode operating gyro-TWA, the guiding center radius of the electron beam is $0.48R$, and the width of electron beam is around $1\,\text{mm}$. The distance between the maximum outer diameter of the electron beam and the copper wall is $1\,\text{mm}$, which can effectively prevent the interception of electrons.
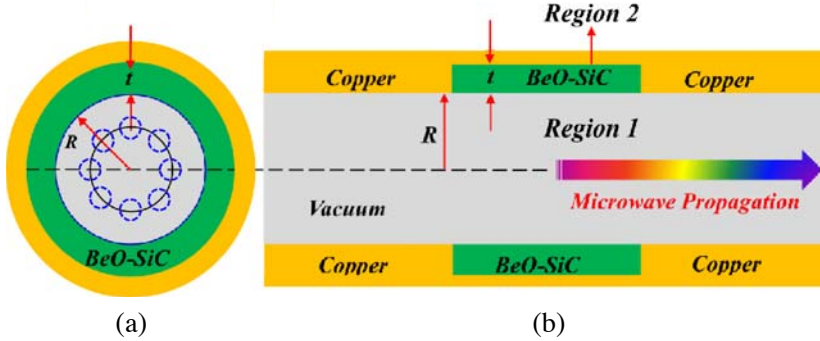

Figure 1. Schematic diagram of the DL circuit, (a) front view and (b) side view.

As shown in Fig. 1, the high lossy dielectric material we used in the gyro-TWA is made of BeO-SiC. In this figure, the inner radius R is $4.3\,\text{mm}$, and t is the lossy material thickness. In this condition, the dispersion curves of the TE_{11}, TE_{21}, and TE_{01} modes in the smooth hollow cylindrical waveguide is shown in Fig. 2. The operating beam voltage and current are $60\,\text{kV}$ and $10\,\text{A}$, respectively, and the beam velocity ratio $\alpha = 1.2$. The operating mode is a cylindrical TE_{01} mode with a center frequency around $48\,\text{GHz}$. And the backward wave oscillations excited from TE_{11} and TE_{21} modes are respectively around $33\,\text{GHz}$ and $38\,\text{GHz}$, which are easy to cause absolute instability.

Potential function method can be used to solve the electromagnetic field distribution, dispersion, and loss properties of each mode in the dielectric loaded waveguide. Let $a = R$, $b = R + t$, based on the boundary condition between region 1 and region 2 and that between Region 2 and the metal wall, we can solve the Helmholtz Equation that the field components satisfies. Refs. [23–26] give a detailed solving process. The eigen equation derived from this is,

$$\left[\frac{1}{k_{\perp 2}}\frac{\epsilon_2}{\epsilon_1}\frac{Q'(k_{\perp 2}a)}{Q(k_{\perp 2}a)} - \frac{1}{k_{\perp 1}}\frac{J_n'(k_{\perp 2}a)}{J_n(k_{\perp 2}a)}\right]\left[\frac{1}{k_{\perp 2}}\frac{\mu_2}{\mu_1}\frac{P'(k_{\perp 2}a)}{P(k_{\perp 2}a)} - \frac{1}{k_{\perp 1}}\frac{J_n'(k_{\perp 2}a)}{J_n(k_{\perp 2}a)}\right]$$

$$-\frac{1}{\epsilon_1\mu_1}\left(\frac{k_z n}{\omega a}\right)^2\left(\frac{1}{k_{\perp 1}^2} - \frac{1}{k_{\perp 1}^2}\right)^2 = 0 \tag{1}$$
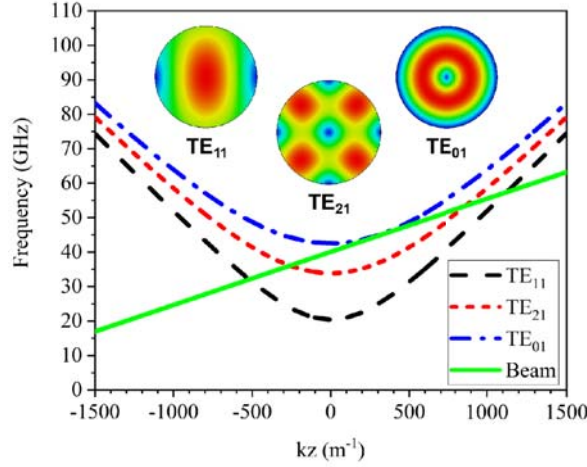
Figure 2. Dispersion diagram of the Q-band TE_{01} gyro-TWA in the smooth hollow waveguide section.

where $k_{\perp 1}$ and $k_{\perp 2}$ are the transverse wave number in the vacuum region and dielectric region, respectively. n is the order of the Bessel functions, and the Bessel function $B_n(k_\perp r)$ is actually a linear combination of the Bessel functions of the 1st kind $J_n(k_\perp r)$ and 2nd kind $N_n(k_\perp r)$

$$P(x) = J_n(x)N_n'(k_{\perp 2b}) - N_n(x)J_n'(k_{\perp 2b}) \tag{2}$$

$$Q(x) = J_n(x)N_n(k_{\perp 2b}) - N_n(x)J_n(k_{\perp 2b}) \tag{3}$$

To solve the tanscendental equation (1), the additional dispersion relation in both regions are required,

$$k_{\perp 1}^2 + k_z^2 = k_1^2 = \omega^2 \epsilon_1 \mu_1 \tag{4}$$

$$k_{\perp 2}^2 + k_z^2 = k_2^2 = \omega^2 \epsilon_2 \mu_2 \tag{5}$$

The dispersion relation (ω, k_z) of the dielectric waveguide could be solved together with Eqs. (1), (2), and (3). The field components are given in the APPENDIX.

When $n = 0$, the dielectric waveguide modes are the pure TE_{0m} or TM_{0m} modes. In order to distinguish it from the empty waveguide, we write it as TE_{0m}^d or TM_{0m}^d modes. Here, "d" denotes the dielectric. When $n \neq 0$, the modes are hybrid modes HE_{nm} or EH_{nm}, and each one has six field components. The same, we write it as HE_{nm}^d or EH_{nm}^d modes. It is worth mentioning that [27, 28]
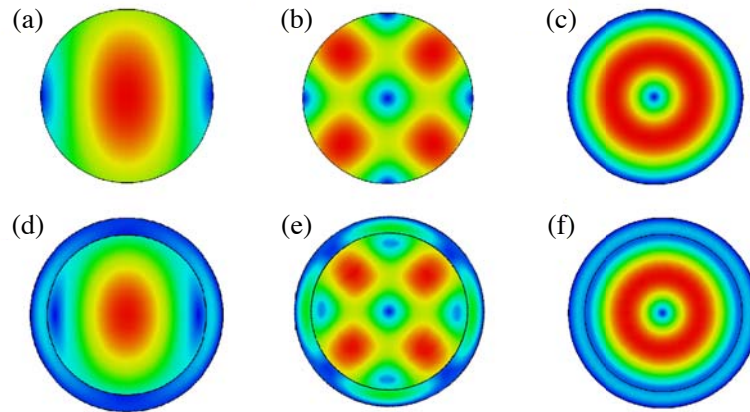

Figure 3. Mode patterns in the DL circuit and smooth hollow waveguide, (a) TE_{11}, (b) TE_{21} and (c) TE_{01}^d modes in the smooth hollow waveguide waveguide. (d) HE_{12}^d, (e) HE_{22}^d and (f) TE_{02}^d modes in the dielectric loaded circular waveguide.

proposed a simple way to distinguish the hybrid waves by using two membrane functions. In some cases, the TE_{11}, TE_{21}, and TE_{01} modes in the smooth hollow waveguide are similar to the HE_{12}^d, HE_{22}^d, and TE_{02}^d modes in the dielectric loaded waveguide as shown in Fig. 3. In Figs. 3(d)–(f), the inner radius $R = 4.3$ mm, and the dielectric thickness $t = 0.9$ mm. In addition, Ref. [29] provided a method for analyzing the modes of an eccentrically dielectric-Loaded circular waveguide that complements the theory of dielectric loaded waveguides.

3. THEORETICAL CALCULATED AND SIMULATED RESULTS

Based on the dielectric theory mentioned above, dispersion and loss properties of the DL circuit from the theoretical calculation and numerical simulation of the HE_{12}^d, HE_{22}^d, and TE_{02}^d modes are respectively presented. The simulated results are obtained by the CST Microwave Studio. Besides, mode patterns of different dielectric thicknesses are also investigated by simulation.

3.1. Dispersion and Loss Properties

Figures 4(a) and (b) respectively plot the theoretically calculated and CST simulated DL circuit dispersion and loss (per centimeter) curves. The dielectric properties are $\epsilon_r = 10.6$ and $\tan\delta = 0.28$, and dielectric thickness $t = 0.9$ mm. In Fig. 4(a), we can find that the dispersion of the TE_{02}^d mode is similar to the TE_{01} mode of the hollow cylindrical waveguide. This feature makes the electron beam and electromagnetic wave meet the synchronizing condition to achieve the beam pre-bunching and wave pre-amplification in the DL circuit. In addition, from Fig. 4(b), we can find that the loss of the TE_{02}^d mode in 40–50 GHz changes from 40 dB/cm to 4 dB/cm. It can help us reduce the risk of the absolute instability. Besides, the losses of the HE_{12}^d and HE_{22}^d modes are higher than 10 dB/cm and 20 dB/cm at 33 GHz and 38 GHz, respectively, where they most likely lead to backward wave oscillations.
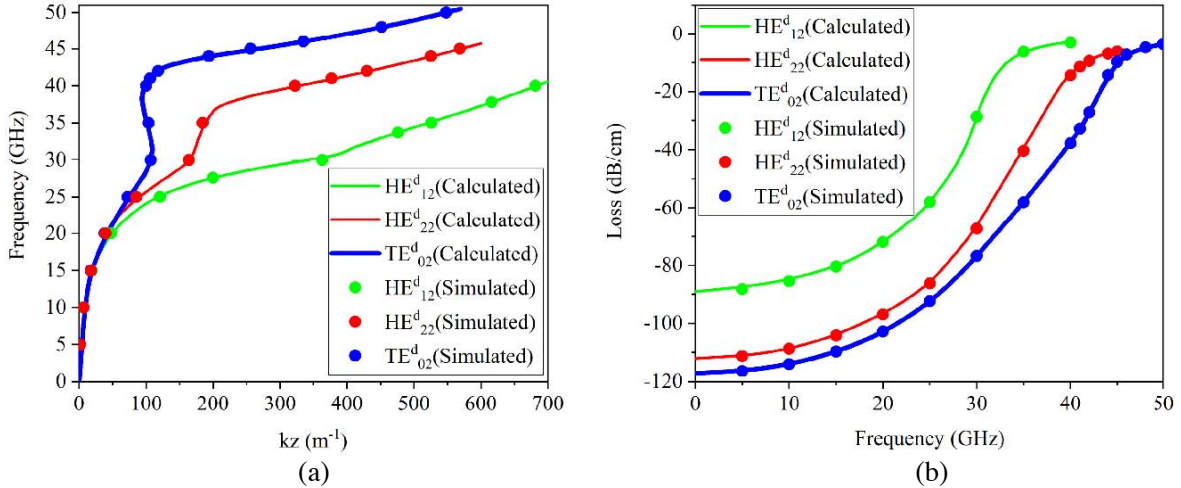

Figure 4. Theoretically calculated and simulated results of the dispersion and loss curves of the HE_{12}^d, HE_{22}^d and TE_{02}^d modes. (a) Dispersion curves, (b) loss curves (dB/cm).

3.2. Dispersion, Loss and Mode Patterns of Different Thickness

Figures 5(a)–(f) respectively give the DL circuit propagation constant kz and loss contour plots of the HE_{12}^d, HE_{22}^d, and TE_{02}^d modes versus dielectric thickness. Obviously, with the increase of dielectric thickness, the DL circuit loss first increases, then decreases, and finally stabilizes at a certain value. Although we found that the highest loss of each mode appeared at a thickness of 0.7 mm, we did not adopt this thickness in our gyro-TWA. In our design, it is necessary to keep the propagation constant
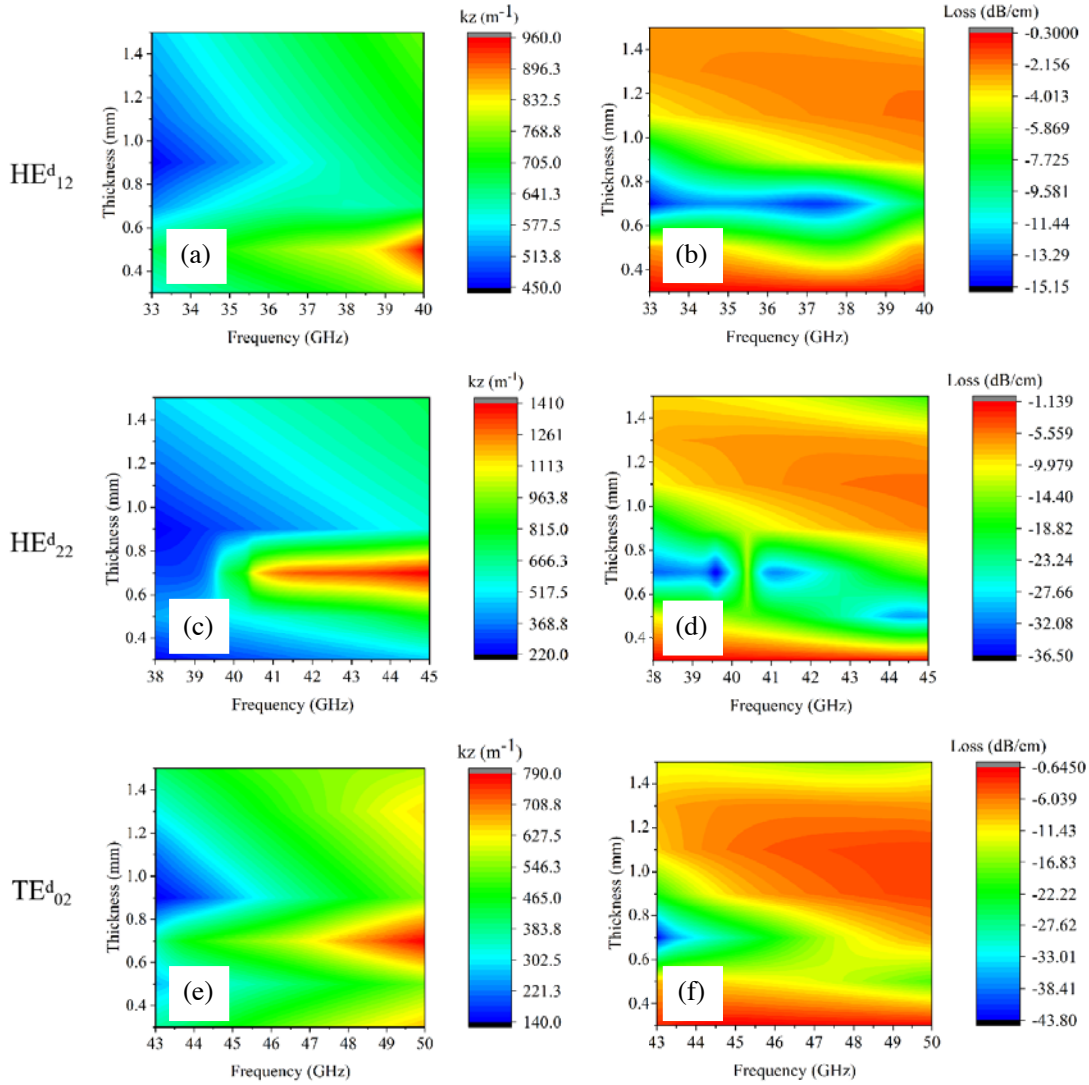
Figure 5. Dispersion and loss properties in different dielectric thickness of the HE_{12}^d, HE_{22}^d and TE_{02}^d modes. (a) and (b) present the dispersion and loss properties of the HE_{12}^d mode. (c) and (d) present the dispersion and loss properties of the HE_{22}^d mode. (e) and (f) present the dispersion and loss properties of the TE_{02}^d mode.

in the DL circuit and hollow cylindrical waveguide close so that the electron beam and millimeter-wave have the best matching condition and then have an effective beam-wave interaction.

Figures 6(a)–(l) respectively give the electric field patterns in the DL circuit excited by corresponding hollow cylindrical waveguide modes with four different dielectric thicknesses: 0.3 mm, 0.7 mm, 0.9 mm, and 1.3 mm. From the mode patterns, we can find the electric field in the thin DL condition, and the excited mode is not a smooth hollow waveguide-like mode. In other words, the field distribution of the HE_{12}^d, HE_{22}^d, and TE_{02}^d modes in the vacuum region of the DL waveguide are not like the TE_{12}, TE_{21}, and TE_{01} in the hollow waveguide. When $t = 0.7$ mm, most of the electric field and mode energy is in the high loss dielectric. In addition, when the field distribution is almost entirely concentrated in the dielectric region, the mode will be converted to a slow wave mode. That is why it shows a large propagation constant and high attenuation in this thickness. However, this mode pattern is not what we expected in the beam-wave interaction, because it may cause a unstable oscillation and disrupt the bunched state of the electron beam. So we choose a dielectric thickness 0.9 mm in our final design.
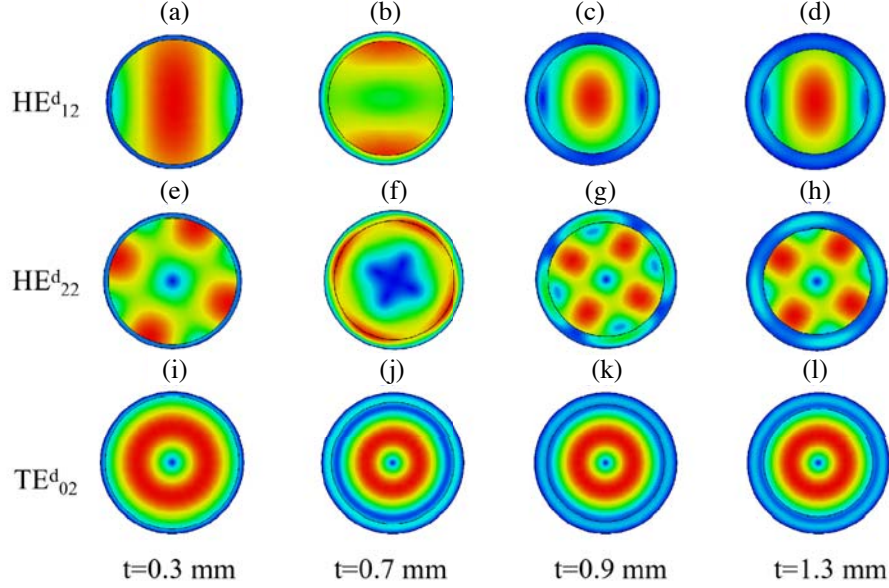
Figure 6. Electric field contour plots of the HE_{12}^d, HE_{22}^d and TE_{02}^d modes with different dielectric thickness. (a)–(d) present the HE_{12}^d mode pattern in the dielectric thickness of 0.3 mm, 0.7 mm, 0.9 mm and 1.3 mm at 33 GHz. (e)–(h) present the $HE^d{}_{22}$ mode pattern in the dielectric thickness of 0.3 mm, 0.7 mm, 0.9 mm and 1.3 mm at 38 GHz. (i)–(l) present the $TE^d{}_{02}$ mode pattern in the dielectric thickness of 0.3 mm, 0.7 mm, 0.9 mm and 1.3 mm at 48 GHz.

From the electric field we obtained, the HE_{12}^d, HE_{22}^d, and TE_{02}^d modes have a great change when the thickness of the dielectric is thin. They exhibit single maximum field strength characteristics in the radial direction. It shows that they degenerate to the HE_{11}^d, HE_{21}^d, and TE_{01}^d modes. When the dielectric thickness is over 0.9 mm, we can find that these DL waveguide modes exhibits double maximum field strength characteristics. One electric peak is in the vacuum region, and the other electric peak is in the high loss dielectric region. Furthermore, in the vacuum region, the field distribution is more like the corresponding TE_{nm} in the hollow waveguide. Meanwhile, the dispersion curves of the DL waveguide modes will be more like those in the empty waveguide. In the gyro-TWA design, we need to consider both dispersion and loss characteristics of each mode to ensure that the tube can work stably under high gain conditions.

4. MILLIMETERWAVE MEASUREMENT AND DISCUSSION

4.1. Dispersion and loss measurement

Figure 7 shows the ceramic rings under test and the corresponding mode converters. Fig. 7(a) shows the dielectric ceramic ring we used in our measurement. stably, respectively [30]. These circular waveguide modes can convert into the corresponding HE_{12}^d, HE_{22}^d and TE_{02}^d modes in the dielectric loaded waveguide. To eliminate the effects of the mode converters, in our measurement, we measured the S-parameters of the ceramic loaded waveguide with two different lengths respectively. Because of the low reflection from the mode converters to the ceramic loaded waveguides, we can make a difference of the transmission and phase between these two measurements to get the dispersion and loss properties of each mode.

Figures 8, 9, and 10 respectively plot the theoretically calculated, simulated, and measured dispersion and loss curves of the HE_{12}^d, HE_{22}^d, and HE_{02}^d modes. The results show the calculation, simulation, and measurement agree very well with each other. From Fig. 8, we can know that the circuit loss and dispersion curves from the theoretical calculation, simulation, and VNA measurement agree very well. The results show that the DL circuit loss for the TE_{11} mode at 33 GHz is 10 dB/cm. Fig. 9(b)
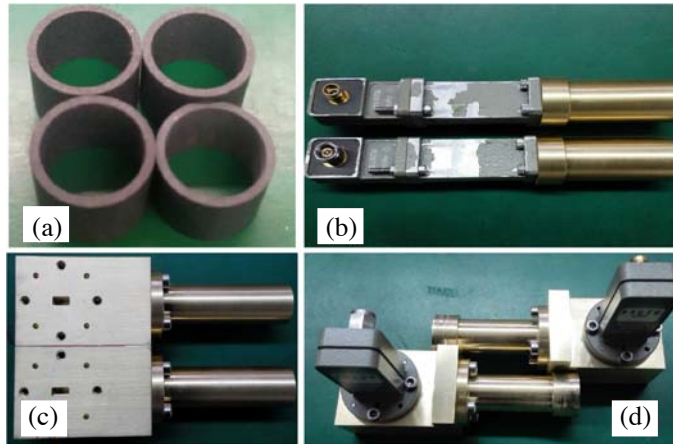
Figure 7. (a) is the dielectric ceramic ring. (b), (c), and (d) are the circular TE_{11}, TE_{21}, and TE_{01} mode converters, respectively.
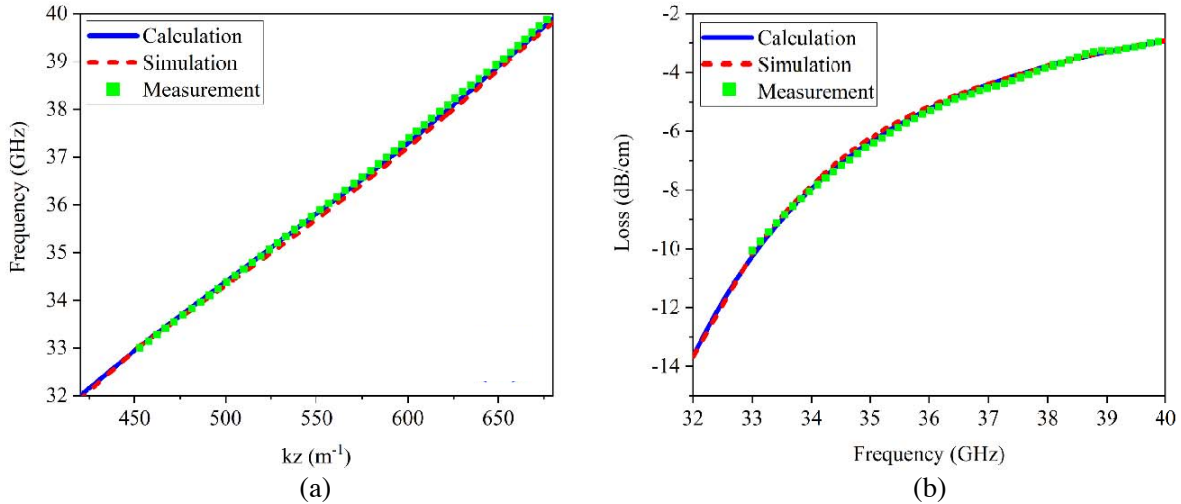

Figure 8. Theoretically calculated, simulated and measured results of (a) the DL circuit loss and (b) dispersion curves of the HE_{12}^d mode in the DL waveguide.

shows that the HE_{22}^d mode loss achieves $22\,dB/cm$ at $38\,GHz$. Fig. 10(b) shows that from $43\,GHz$–$50\,GHz$, the mode loss achieves $22\,dB/cm$–$3.7\,dB/cm$. At the center operating frequency $48\,GHz$, the mode loss is around $5\,dB/cm$. This performance is sufficient to ensure the stable operation of our gyro-TWA.

4.2. DL Waveguide Mode Pattern Measurement

To effectively understand the electric field distribution of DL waveguide modes, we measure the near field distribution using a moving scanning platform. In our designed gyro-TWA, from the dispersion curves, the intersection point of the electron and HE_{22}^d and TE_{02}^d modes are near the cutoff frequency, and it is more easy to cause oscillations. In contrast, the propagation constant kz of the HE_{12}^d is larger at the intersection point, and the resulting oscillation is easier to suppress. Thus, we focused on testing the field distribution of the HE_{22}^d and TE_{02}^d modes. The flowchart of the measurement is shown in Fig. 11. A certain power and frequency signal is generated by the single generator and amplified by the solid state power amplifier. Through a mode converter, it converts to a specific DL waveguide mode
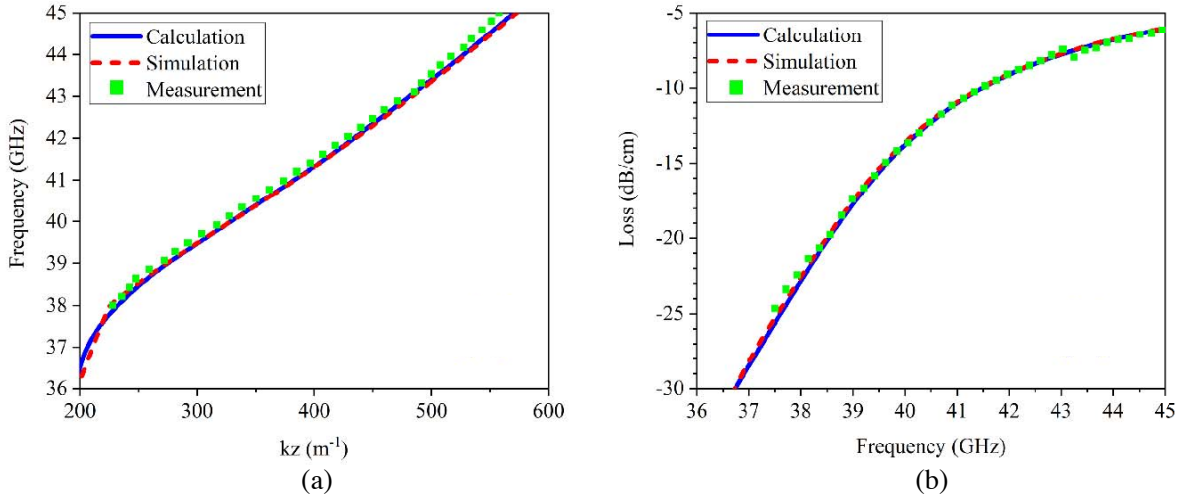
Figure 9. Theoretically calculated, simulated and measured results of (a) the DL circuit loss and (b) dispersion curves of the HE_{22}^d mode in the DL waveguide.

Figure 10. Theoretically calculated, simulated and measured results of (a) the DL circuit loss and (b) dispersion curves of the TE_{02}^d mode in the DL waveguide.
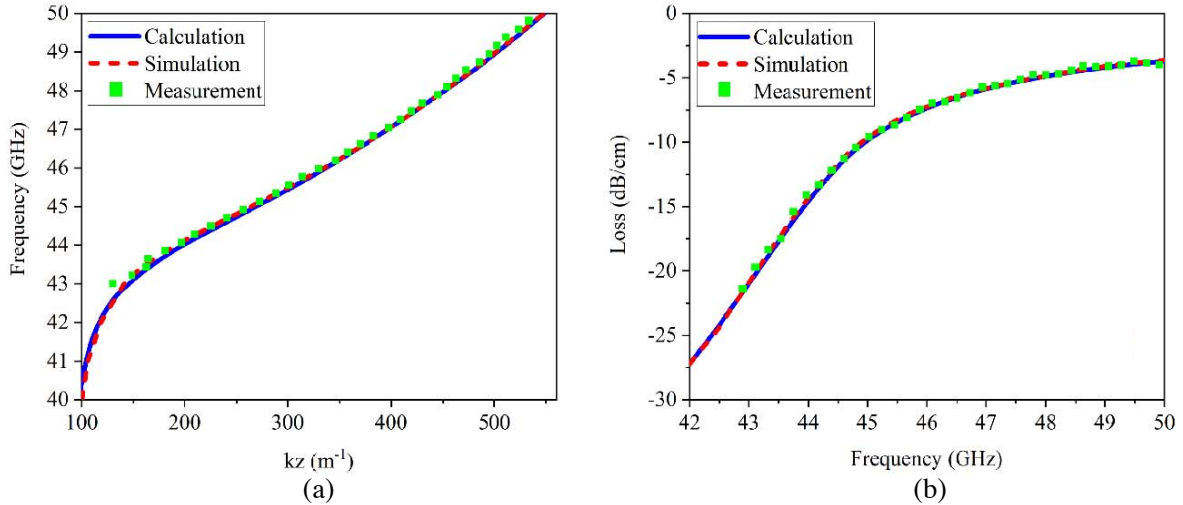
under measurement. The detector is composed of program-controlled movable support and a rectangular waveguide, which is used to receive the near radiation field. By slowly moving the rectangular waveguide, we can achieve near-field scanning. In order to reduce the impact of environmental reflections, absorbing materials are laid around the measurement platform. Finally, the two-dimensional field map is obtained through the post-processing algorithm.

Figures 12(a) and (b) show the measured and simulated results of the near field of the HE_{22}^d mode. In our measurement, the distance between the waveguide port and the detector is 3 mm. From this figure, we can find obvious periodic properties, which are consistent with the HE_{22}^d mode property. In our measurement, because the detector used to receive the radiation field is a rectangular waveguide, the reflection caused by the wall thickness of the waveguide will have a certain impact on the test structure. Besides, rectangular waveguide can just receive the transverse component of electric field. Considering the measurement error, the simulation and measurement results are in good agreement. The experimental verification of the field distribution further ensures the dispersion and loss characteristics.
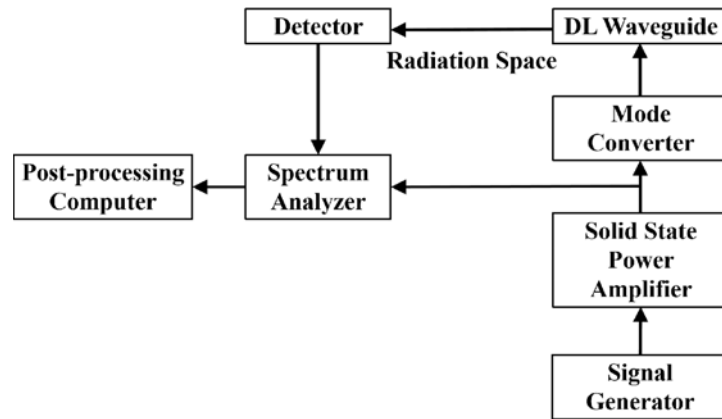
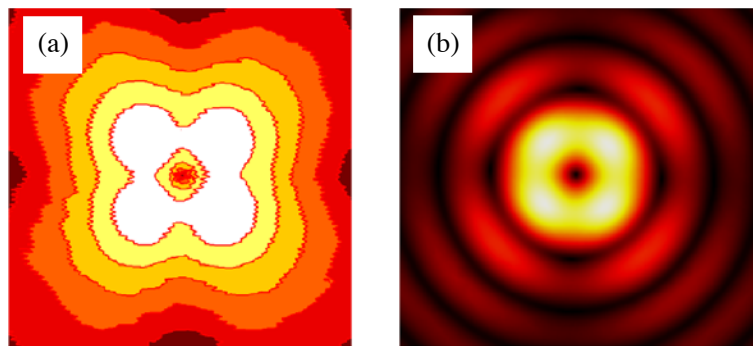**Figure 11.** Flow chart of the near field measurement.

Figure 12. Near field distribution of the HE_{22}^d mode. (a) Measured result. (b) Simulated result.
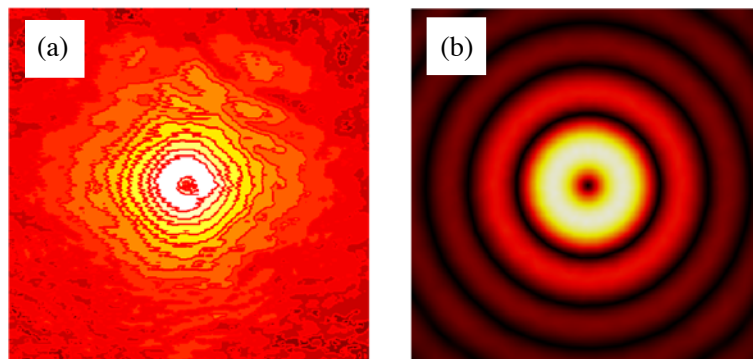

Figure 13. Near field distribution of the TE_{02}^d mode. (a) Measured result. (b) Simulated result.

With our best regards, Figures 13(a) and (b) show the measured and simulated results about the near field distribution of the TE_{02}^d mode, respectively. Because the TE_{02}^d mode will spread evenly around in free space, the field distribution in the space presents a ring with decreasing intensity layer by layer. In Fig. 16(a), we find that the measured field presents some local irregular peaks, because the receiving waveguide with a certain metal wall thickness will produce reflections. Considering the measurement error, simulation and measurement results are in good agreement. The experimental verification of the field distribution further ensures the dispersion loss characteristics of this mode.

5. CONCLUSION

This paper comprehensively introduces the mode characteristics of the high-loss dielectric loaded waveguide in gyro-TWA from the aspects of theory, simulation, and measurement. The operating and parasitic modes of HE_{12}^d, HE_{22}^d, and TE_{02}^d are respectively investigated. The results show good agreement of the theory calculation, simulation, and measurement, and it can meet the design requirements of our gyro-TWA. The study is of great importance for the backward wave and self oscillations suppression and working stability in a gyro-TWA design.

ACKNOWLEDGMENT

APPENDIX A. EXPRESSION OF FIELD DISTRIBUTION IN DIELECTRIC LOADED WAVEGUIDE

The field components are given as follows:
    Vacuum Region:

$$E_z = -jA(z)\chi J_n(k_{\perp 1}r)e^{j(\omega t-n\varphi)} \tag{A1}$$

$$H_z = A(z)J_n(k_{\perp 1}r)e^{j(\omega t-n\varphi)} \tag{A2}$$

$$E_r = \left[-A(z)\frac{n}{r}\frac{\omega\mu_1}{k_{\perp 1}^2}J_n(k_{\perp 1}r) - jA'(z)\frac{1}{k_{\perp 1}}\chi J_n'(k_{\perp 1}r)\right]e^{j(\omega t-n\varphi)} \tag{A3}$$

$$E_\varphi = \left[jA(z)\frac{\omega\mu_1}{k_{\perp 1}}J_n'(k_{\perp 1}r) - A'(z)\frac{n}{r}\frac{1}{k_{\perp 1}^2}\chi J_n(k_{\perp 1}r)\right]e^{j(\omega t-n\varphi)} \tag{A4}$$

$$H_r = \left[A'(z)\frac{1}{k_{\perp 1}}J_n'(k_{\perp 1}r) - jA'(z)\frac{n}{r}\frac{\omega\epsilon_1}{k_{\perp 1}^2}\chi J_n(k_{\perp 1}r)\right]e^{j(\omega t-n\varphi)} \tag{A5}$$

$$H_\varphi = \left[-jA'(z)\frac{n}{k_{\perp 1}^2 r}J_n(k_{\perp 1}r) - A(z)\frac{\omega\epsilon_1}{k_{\perp 1}}\chi J_n'(k_{\perp 1}r)\right]e^{j(\omega t-n\varphi)} \tag{A6}$$

    Dielectric Region

$$E_z = -jA(z)\left[\bar{\alpha}J_n(k_{\perp 2}r) + \bar{\beta}N_n(k_{\perp 2}r)\right]e^{j(\omega t-n\varphi)} \tag{A7}$$

$$H_z = A(z)\left[\alpha J_n(k_{\perp 2}r) + \beta N_n(k_{\perp 2}r)\right]e^{j(\omega t-n\varphi)} \tag{A8}$$

$$E_r = \Bigl[-A(z)\frac{n}{r}\frac{\omega\mu_2}{k_{\perp 2}^2}(\alpha J_n(k_{\perp 2}r) + \beta N_n(k_{\perp 2}r))$$
$$-jA'(z)\frac{1}{k_{\perp 2}}(\bar{\alpha}J_n'(k_{\perp 2}r) + \bar{\beta}N_n'(k_{\perp 2}r))\Bigr]e^{j(\omega t-n\varphi)} \tag{A9}$$

$$E_\varphi = \Bigl[-jA'(z)\frac{\omega\mu_2}{k_{\perp 2}}(\alpha J_n'(k_{\perp 2}r) + \beta N_n'(k_{\perp 2}r))$$
$$-A'(z)\frac{n}{r}\frac{1}{k_{\perp 2}^2}(\bar{\alpha}J_n(k_{\perp 2}r) + \bar{\beta}N_n(k_{\perp 2}r))\Bigr]e^{j(\omega t-n\varphi)} \tag{A10}$$

$$H_r = \Bigl[A'(z)\frac{1}{k_{\perp 2}}(\alpha J_n'(k_{\perp 2}r) + \beta N_n'(k_{\perp 2}r))$$
$$-jA(z)\frac{n}{r}\frac{\omega\epsilon_2}{k_{\perp 2}^2}(\bar{\alpha}J_n(k_{\perp 2}r) + \bar{\beta}N_n(k_{\perp 2}r))\Bigr]e^{j(\omega t-n\varphi)} \tag{A11}$$

$$
\begin{aligned}
H_\varphi = \Bigg[&- jA'(z)\frac{n}{r}\frac{1}{k_{\perp 2}^2}(\alpha J_n(k_{\perp 2}r) + \beta N_n(k_{\perp 2}r)) \\
&- A(z)\frac{n}{r}\frac{\omega\epsilon_2}{k_{\perp 2}^2}(\bar{\alpha}J_n'(k_{\perp 2}r) + \bar{\beta}N_n'(k_{\perp 2}r)) \Bigg] e^{j(\omega t - n\varphi)}
\end{aligned}
\tag{A12}
$$

where $A(z)$ is the axial field amplitude, and other constants are given as follows:

$$
\alpha = \frac{J_n(k_{\perp 1}a)N_n'(k_{\perp 2}b)}{P(k_{\perp 2}a)}
\tag{A13}
$$

$$
\beta = \frac{J_n(k_{\perp 1}a)J_n'(k_{\perp 2}b)}{Q(k_{\perp 2}a)}
\tag{A14}
$$

$$
\chi = -\frac{\omega\mu_2 a}{k_z n(k_{\perp 2}^2 - k_{\perp 1}^2)}\left[k_{\perp 1}k_{\perp 2}^2\frac{\mu_1}{\mu_2}\frac{J_n'(k_{\perp 1}a)}{J_n(k_{\perp 1}a)} - k_{\perp 2}k_{\perp 1}^2\frac{P_n'(k_{\perp 2}a)}{P_n(k_{\perp 2}a)}\right]
\tag{A15}
$$

$$
\bar{\alpha} = \chi\frac{J_n(k_{\perp 1}a)N_n(k_{\perp 2}b)}{Q(k_{\perp 2}a)}
\tag{A16}
$$

$$
\bar{\beta} = -\chi\frac{J_n(k_{\perp 1}a)J_n(k_{\perp 2}b)}{Q(k_{\perp 2}a)}
\tag{A17}
$$

REFERENCES

1. Chu, K. R., "The electron cyclotron maser," *Rev. Mod. Phys.*, Vol. 6, No. 2, 489–540, Apr. 2004.

2. Garven, M., J. P. Calame, B. G. Danly, K. T. Nguyen, B. Levush, F. N. Wood, and D. E. Pershing, "A gyrotron-traveling-wave tube amplifier experiment with a ceramic loaded interaction region," *IEEE Trans. Plasma Sci.*, Vol. 30, No. 3, 885–893, Apr. 2002.

3. Du, C. H., T. H. Chang, P. K. Liu, Y. C. Huang, P. X. Jiang, S. X. Xu, Z. H. Geng, B. L. Hao, L. Xiao, G. F. Liu, Z. D. Li, and S. H. Shi, "Design of a W-band gyro-TWT amplifier with a lossy ceramic-loaded circuit," *IEEE Trans. on Electron Devices*, Vol. 60, No. 7, 2388–2395, Jul. 2013.

4. Song, H. H., D. B. McDermott, Y. Hirata, L. R. Barnett, C. W. Domier, H. L. Hsu, T. H. Chang, W. C. Tsai, K. R. Chu, and N. C. Luhmann, "Theory and experiment of a 94 GHz gyrotron traveling-wave amplifier," *Plys. Plasma*, Vol. 11, No. 5, 2935–2941, May 2004.

5. Yan, R., Y. Luo, G. Liu, and Y. L. Pu, "Design and experiment of a Q-band gyro-TWT loaded with lossy dielectric," *IEEE Trans. on Electron Devices*, Vol. 59, No. 12, 3612–3617, Dec. 2012.

6. Yan, R., et al., "Investigation on high average power operations of gyro-TWTs with dielectric-Loaded waveguide circuits," *IEEE Trans. on Electron Devices*, Vol. 65, No. 7, 3012–3018, Jul. 2018.

7. He, W., C. R. Donaldson, L. Zhang, K. Ronald, P. McElhinney, and A. W. Cross, "High power wideband gyrotron backward wave oscillator operating towards the terahertz region," *Phys. Rev. Lett.*, Vol. 90, No. 25, 258–302, Jul. 2003.

8. Samsonov, S. V., I. G. Gachev, G. G. Denisov, et al., "Ka-band gyrotron travelling wave tube with the highest continuous wave and average power," *IEEE Trans. on Electron Devices*, Vol. 61, No. 12, 4264–4267, Dec. 2014.

9. Samsonov, S. V., G. G. Denisov, I. G. Gachev, and A. A. Bogdashov, "CW operation of a W-band high-gain helical-waveguide gyrotron traveling-wave tube," *IEEE Electron Device Letters*, Vol. 41, No. 5, 773–776, May 2020.

10. Rozental, M., et al., "CW multifrequency K-band source based on a helical-waveguide gyro-TWT with delayed feedback," *IEEE Trans. on Electron Devices*, Vol. 68, No. 1, 330–335, Jan. 2021.

11. Kim, H. J., E. A. Nanni, M. A. Shapiro, J. R. Sirigiri, P. P. Woskov, and R. J. Temkin, "Amplification of picosecond pulses in a 140-GHz gyrotron-traveling wave tube," *Phys. Rev. Lett.*, Vol. 110, 165101-1–165101-5, Apr. 2013.

12. Nanni, E. A., S. M. Lewis, M. A. Shapiro, R. G. Griffin, and R. J. Temkin, "Photonic-band-gap traveling-wave gyrotron amplifier," *Phys. Rev. Lett.*, Vol. 111, 235101-1–235101-5, Dec. 2013.

13. Chu, K. R., et al., "Theory and experiment of ultrahigh-gain gyrotron traveling wave amplifier," *IEEE Trans. Plasma Sci.*, Vol. 27, No. 2, 391–404, Apr. 1999.

14. Yan, R., Y. Tang, and Y. Luo, "Design and experimental study of a high-gain W-Band gyro-TWT with nonuniform periodic dielectric loaded waveguide," *IEEE Trans. on Electron Devices*, Vol. 61, No. 7, 2564–2569, Jul. 2014.

15. Yeh, Y. S., C. L. Hung, T. H. Chang, et al., "A study of a terahertz gyrotron traveling-wave amplifier," *Plys. Plasma*, Vol. 24, 103126, Oct. 2017.

16. Yeh, Y. S., C. L. Hung, T. H. Chang, Y. W. Guo, B. H. Kao, C. H. Chen, and Z. W. Wang, "Low-voltage harmonic multiplying gyrotron traveling-wave amplifier in G band," *Plys. Plasma*, Vol. 22, 123115, Dec. 2015.

17. Du, C. H., S. Pan, H. Q. Bian, and P. K. Liu, "Time-domain multimode analysis of a terahertz gyro-TWT amplifier," *IEEE Trans. on Electron Devices*, Vol. 65, No. 4, 1550–1557, Apr. 2014.

18. Wang, J. X., Y. Luo, Y. Xu, R. Yan, Y. L. Pu, X. Deng, and H. Wang, "Simulation and experiment of a Ku-band gyro-TWT," *IEEE Trans. on Electron Devices*, Vol. 61, No. 6, 1818–1823, Jun. 2014.

19. Tang, Y., Y. Luo, Y. Xu, R. Yan, W. Jiang, and Y. Zheng, "Design of a novel dual-band gyro-TWT," *IEEE Trans. on Electron Devices*, Vol. 61, No. 11, 3858–3863, Nov. 2014.

20. Rao, W., L. Wang, Y. Wang, C. Fang, G. Liu, W. Jiang, J. X. Wang, Z. W. Wu, F. Y. Zhang, and Y. Luo, "Design of a high-gain X-band megawatt gyrotron traveling-wave tube," *IEEE Trans. Plasma Sci.*, Vol. 47, No. 6, 2818–2822, Jun. 2019.

21. Li, H., J. X. Wang, Y. L. Yao, and Y. Luo, "Development of high-efficiency gyro-TWT with a nonuniform dielectric-loaded circuit," *IEEE Trans. on Electron Devices*, Vol. 66, No. 6, 2764–2770, Jun. 2019.

22. Li, Y., R. Yan, Y. L. Yao, Q. Q. Yue, X. W. Lin, W. X. Li, G. Liu, and Y. Luo, "Analysis of phase characteristics of gyrotron traveling-wave tubes," *IEEE Trans. on Electron Devices*, Vol. 67, No. 5, 2170–2175, May 2020.

23. Harrington, R. F., *Time Harmonic Electromagnetic Fields*, McGraw-Hill Book Co., New York, 1961.

24. Marcatili, E. A. J. and R. A. Schmeltzer, "Hollow metallic and dielectric waveguides for long distance optical transmission and lasers," *Bell System Tech. J.*, 1783–1809, Jul. 1964.

25. Lee, C. S., S. W. Lee, and S. L. Chuang, "Normal modes in an overmoded circular waveguide coated with lossy material," *IEEE Trans. on Microwave Theory and Techniques*, Vol. 34, No. 7, 773–785, Jul. 1986.

26. Du, C. H. and P. K. Liu, *Millimeter-wave Gyrotron Traveling-wave Tube Ampliers*, 1st Edition, 210, Springer Berlin Heidelberg, 2014.

27. Shcherbinin, V. I., et al., "HE and EH hybrid waves in a circular dielectric waveguide with an anisotropic impedance surface," *Problems of Atomic Science and Technology. Plasma Electronics and New Methods of Acceleration*, Vol. 98, 89–93, 2015.

28. Shcherbinin, V. I., G. I. Zaginaylov, and V. I. Tkachenko, "Analogy between circular core-cladding and impedance waveguides and their membrane functions," *Progress In Electromagnetics Research M*, Vol. 53, 111–120, 2017.

29. Gholizadeh, M. and F. Hojjat Kashani, "A new analytical method for calculating the cutoff frequencies of an eccentrically dielectric-loaded circular waveguide," *IEEE Microwave and Wireless Components Letters*, Vol. 30, No. 5, 453–456, 2016.

30. Liu, G., Y. Wang, Y. L. Pu, et al., "Design and microwave measurement of a novel compact TE0n/TE1n mode converter," *IEEE Trans. on Microwave Theory and Techniques*, Vol. 64, No. 12, 4108–4116, 2016.